1 # Back-calculation of the 2017 Piz Cengalo-Bondo landslide cascade with
2 # r.avaflow

3 *Martin Mergili[1,2], Michel Jaboyedoff[3], José Pullarello[3], Shiva P. Pudasaini[4],*

4 [1] Institute of Applied Geology, University of Natural Resources and Life Sciences (BOKU), Peter-Jordan-Straße 82,
5 1190 Vienna, Austria

6 [2] Geomorphological Systems and Risk Research, Department of Geography and Regional Research, University of Vi-
7 enna, Universitätsstraße 7, 1010 Vienna, Austria

8 [3] Institute of Earth Sciences, University of Lausanne, Quartier UNIL-Mouline, Bâtiment Géopolis, 1015 Lausanne,
9 Switzerland

10 [4] Institute of Geosciences and Meteorology, Geophysics Section, University of Bonn, Meckenheimer Allee 176, 53115
11 Bonn, Germany

12 Correspondence to: M. Mergili (martin.mergili@boku.ac.at)

13 ## Abstract

14 In the morning of 23 August 2017, around 3 million m³ of granitoid rock broke off from the east face of Piz Cengalo,
15 SE Switzerland. The initial rock slide-rock fall entrained 0.6 million m³ of a glacier and continued as a rock(-ice) ava-
16 lanche, before evolving into a channelized debris flow that reached the village of Bondo at a distance of 6.5 km after a
17 couple of minutes. Subsequent debris flow surges followed in the next hours and days. The event resulted in eight
18 fatalities along its path and severely damaged Bondo. The most likely candidates for the water causing the transfor-
19 mation of the rock avalanche into a long-runout debris flow are the entrained glacier ice and water originating from
20 the debris beneath the rock avalanche. In the present work we try to reconstruct conceptually and numerically the
21 cascade from the initial rock slide-rock fall to the first debris flow surge and thereby consider two scenarios in terms
22 of qualitative conceptual process models: (i) entrainment of most of the glacier ice by the frontal part of the initial
23 rock slide-rock fall and/or injection of water from the basal sediments due to sudden rise in pore pressure, leading to a
24 frontal debris flow, with the rear part largely remaining dry and depositing mid-valley; and (ii) most of the entrained
25 glacier ice remaining beneath/behind the frontal rock avalanche, and developing into an avalanching flow of ice and
26 water, part of which overtops and partially entrains the rock avalanche deposit, resulting in a debris flow. Both sce-
27 narios can be numerically reproduced with the two-phase mass flow model implemented with the simulation software
28 r.avaflow, based on plausible assumptions of the model parameters. However, these simulation results do not allow to
29 conclude on which of the two scenarios is the more likely one. Future work will be directed towards the application of
30 a three-phase flow model (rock, ice, fluid) including phase transitions, in order to better represent the melting of glac-
31 ier ice, and a more appropriate consideration of deposition of debris flow material along the channel.

32 Keywords: Debris flow, Entrainment, High-mountain process chain, Rock avalanche, Two-phase flow model,
33 r.avaflow

1 Introduction

Landslides lead to substantial damages to life, property, and infrastructures every year. Whereas initial landslides in hilly terrain have mostly local effects, landslides in high-mountain areas, with elevation differences of thousands of metres over a few kilometres may form the initial points of process chains which, due to their interactions with glacier ice, snow, lakes, or basal material, sometimes evolve into long-runout debris avalanches, debris flows or floods. Such complex landslide events may occur in remote areas, such as the 2012 Alpl rock-snow avalanche in Austria (Preh and Sausgruber, 2015) or the 2012 Santa Cruz multi-lake outburst event in Peru (Mergili et al., 2018a). If they reach inhabited areas, such events lead to major destruction even several kilometres away from the source and have led to major disasters in the past, such as the 1949 Khait rock avalanche-loess flow in Tajikistan (Evans et al., 2009b); the 1962 and 1970 Huascarán rock fall-debris avalanche events in Peru (Evans et al., 2009a; Mergili et al., 2018b); the 2002 Kolka-Karmadon ice-rock avalanche in Russia (Huggel et al., 2005); the 2012 Seti River debris flood in Nepal (Bhandari et al., 2012); or the 2017 Piz Cengalo-Bondo rock avalanche-debris flow event in Switzerland. The initial fall or slide sequences of such process chains are commonly related to a changing cryosphere such as glacial debuttressing, the formation of hanging glaciers, or a changing permafrost regime (Alean, 1985; Haeberli, 1992; Haeberli et al., 1997, 2016; Huggel et al., 2003, 2010, 2012; Noetzli et al., 2006; Gruber and Haeberli, 2007; Harris et al., 2009; Ravanel and Deline, 2011; Krautblatter et al., 2013; Evans and Delaney, 2014; Haeberli and Whiteman, 2014).

Computer models assist risk managers in anticipating the impact areas, energies, and travel times of complex mass flows. They may also support the confirmation or rejection of conceptual models with regard to the physical mechanisms involved in specific cases and thereby contribute to a better understanding of the processes involved. Conventional single-phase flow models, considering a mixture of solid and fluid components (e.g. Voellmy, 1955; Savage and Hutter, 1989; Iverson, 1997; McDougall and Hungr, 2004; Christen et al., 2010), do not serve for such a purpose. Instead, simulations rely on (i) model cascades, changing from one approach to the next at each process boundary (Schneider et al., 2014; Somos-Valenzuela et al., 2016); or (ii) two- or even multi-phase flow models (Pitman and Le, 2005; Pudasaini, 2012; Mergili et al., 2017). Worni et al. (2014) have highlighted the advantages of (ii) for considering also the process interactions and boundaries. Two- or multi-phase flow models separately consider the solid and the fluid phase, but also phase interactions.

The aim of the present work is to learn about our ability to reproduce sophisticated transformation mechanisms involved in complex, cascading landslide processes, with GIS-based numerical models. For this purpose, we apply the computational tool r.avaflow (Mergili et al., 2017), which employs an enhanced version of the Pudasaini (2012) two-phase flow model, to back-calculate the 2017 Piz Cengalo-Bondo landslide cascade in SE Switzerland, which was characterized by the transformation of a rock avalanche to a long-runout debris flow. We consider two scenarios in terms of hypothetic qualitative conceptual models of the physical transformation mechanisms. On this basis, we try to numerically reproduce these scenarios, satisfying the requirements of physical plausibility of the model parameters, and empirical adequacy in terms of correspondence of the results with the documented and inferred impact areas, vol-

68   umes, velocities, and travel times. Based on the outcomes, we identify the key challenges to be addressed in future

69   research.

70   Thereby we rely on the detailed description, documentation, and topographic reconstruction of this recent event. The

71   event documentation, data used, and the conceptual models are outlined in Section 2. We briefly introduce the simu-

72   lation framework r.avaflow (Section 3) and explain its parametrization and our simulation strategy (Section 4) before

73   presenting (Section 5) and discussing (Section 6) the results obtained. Finally, we conclude with the key messages of

74   the study (Section 7).

2   The 2017 Piz Cengalo-Bondo landslide cascade

2.1   Piz Cengalo and Val Bondasca

77   The Val Bondasca is a left tributary valley to the Val Bregaglia in the canton of the Grisons in SE Switzerland (Fig. 1).

78   The Bondasca stream joins the Mera River at the village of Bondo at 823 m asl. It drains part of the Bregaglia Range,

79   built up by a mainly granitic intrusive body culminating at 3678 m asl. Piz Cengalo, with a summit elevation of

80   3368 m asl, is characterized by a steep, intensely fractured NE face which has repeatedly been the scene of landslides,

81   and which is geomorphologically connected to the Val Bondasca through a steep glacier forefield. The glacier itself has

82   largely retreated to the cirque beneath the rock wall.

83   On 27 December 2011, a rock avalanche with a volume of 1.5–2 million m³ developed out of a rock toppling from the

84   NE face of Piz Cengalo, travelling for a distance of 1.5 km down the Val Bondasca (Haeberli et al., 2013; De Blasio and

85   Crosta, 2016; Amann et al., 2018). No entrainment of glacier ice was documented for this event, and the deposit did

86   not connect to the main channel of Val Bondasca, so that no debris flow was recorded and the village of Bondo re-

87   mained unaffected. As blue ice had been observed directly at the scarp, the role of permafrost for the rock instability

88   was discussed. An early warning system was installed and later extended (Steinacher et al., 2018). Displacements at the

89   scarp area were few centimetres per year between 2012 and 2015, and accelerated in the following years. In early Au-

90   gust 2017, increased rock fall activity and deformation rates alerted the authorities. A major rock fall event occurred

91   on 21 August 2017 (Amann et al., 2018).

2.2   The event of 23 August 2017

93   At 9:31 am local time on 23 August 2017, a volume of 3.1–3.5 million m³ detached from the NE face of Piz Cengalo, as

94   indicated by WSL (2017); Amann et al. (2018); and the point cloud we obtained through structure from motion using

95   pictures taken after the event. Documented by videos and by seismic records (Walter et al., 2018), it evolved into a

96   rock avalanche which impacted the glacier beneath the rock face and entrained approx. 0.6 million m³ of ice (VAW,

97   2017; WSL, 2017). Part of the rock avalanche immediately converted into a debris flow which flowed down the Val

98   Bondasca. It was detected at 9:34 by the debris flow warning system which had been installed near the hamlet of Prä

99   approx. 1 km upstream from Bondo. According to different sources, the debris flow surge arrived at Bondo between

100 9:42 (derived from WSL, 2017) and 9:48 (Amt für Wald und Naturgefahren, 2017). The rather low velocity in the low-

101 er portion of the Val Bondasca is most likely a consequence of the narrow gorge topography, and of the viscous behav-

102 iour of this first surge. Whereas approx. 540,000 m³ of material were involved, only 50,000 m³ arrived at Bondo im-

103 mediately (WSL, 2017). The remaining material was partly remobilized by six further debris flow surges recorded dur-

104 ing the same day, one on 25 August, and one – triggered by rainfall – on 31 August 2017. All nine surges together de-

105 posited a volume of approx. 500,000–800,000 m³ in the area of Bondo, less than half of which was captured by a reten-

106 tion basin (Bonanomi and Keiser, 2017).

107 The total angle of reach of the process chain from the initial release down to the village of Bondo was approx. 18°,

108 computed from the travel distance of 7.2 km and the vertical drop of approx. 2.3 km. The initial landslide to the ter-

109 minus of the rock avalanche showed an angle of reach of approx. 28°, derived from the travel distance of 3.3 km and

110 the vertical drop of 1.8 km. There were eight fatalities, concerning hikers in the Val Bondasca, extensive damages to

111 buildings and infrastructures, and evacuations for several weeks or even months.

112 **2.3   Data and conceptual model**

113 Reconstruction of the rock and glacier volumes involved in the event was based on an overlay of a 2011 swisstopo

114 MNS-Digital Elevation Model (DEM) (contract: swisstopo–DV084371), derived through airborne laser scanning in

115 2011 and available at a raster cell size of 2 m, and a Digital Surface Model (DSM) obtained through Structure from

116 Motion (SfM) techniques after the 2017 event. This analysis resulted in a detached rock volume of 3.5 million m³,

117 which is slightly more than the value of 3.15 million m³ reported by Amann et al. (2018), and an entrained ice volume

118 of 770,000 m³ (Fig. 4). However, these volumes neglect smaller rock falls before and after the large 2017 event, and

119 also glacial retreat. The 2011 event took place after the DTM had been acquired, but it released from an area above the

120 2017 scarp and does therefore not affect the volume reconstruction. Assuming some minor entrainment of the glacier

121 ice in 2011 and some glacial retreat, we arrive at an entrained ice volume of 600,000 m³, a value which is very well

122 supported by VAW (2017).

123 There is still disagreement on the origin of the water having led to the debris flow, particularly to the first surge. Bo-

124 nanomi and Keiser (2017) clearly mention meltwater from the entrained glacier ice as the main source, whereby much

125 of the melting is assigned to impact, shearing and frictional heating directly at or after impact, as it is often the situa-

126 tion in rock-ice avalanches (Pudasaini and Krautblatter, 2014). WSL (2017) has shown, however, that the energy re-

127 leased was only sufficient to melt approx. half of the glacier ice. Water pockets in the glacier or a stationary water

128 source along the path might have played an important role (Demmel, 2019). Walter et al. (2019) claim that much of

129 the glacier ice was crushed, ejected and dispersed (Fig. 3b), whereas water injected into the rock avalanche due to pore

130 pressure rise in the basal sediments would have played a major role. In any case, the development of a debris flow

131 from a landslide mass with an overall solid fraction of as high as ~0.85 (considering the water equivalent of the glacier

132 ice) requires some spatio-temporal differentiation of the water/ice content. We consider two qualitative conceptual

133 models – or scenarios – possibly explaining such a differentiation:

134   A. The initial rock slide-rock fall led to massive entrainment, fragmenting and melting of glacier ice, mixing of
135   rock with some of the entrained ice and the meltwater, and injection of water from the basal sediments into
136   the rock avalanche mass quickly upon impact due to overload-induced pore pressure rise. As a consequence,
137   the front of the rock avalanche was characterized by a high content of ice and water, highly mobile, and
138   therefore escaped as the first debris flow surge, whereas the less mobile rock avalanche behind – still with
139   some water and ice in it – decelerated and deposited mid-valley. The secondary debris flow surges occurred
140   mainly due to backwater effects. This scenario largely follows the explanation of Walter et al. (2019) that the
141   first debris flow surge was triggered at the front of the rock avalanche by overload and pore pressure rise,
142   whereas the later surges overtopped the rock avalanche deposits, as indicated by the surficial scour patterns.

143   B. The initial rock slide-rock fall impacted and entrained the glacier. Most of the entrained ice remained beneath
144   and developed into an avalanching flow of melting ice behind the rock avalanche. The rock avalanche decel-
145   erated and stopped mid-valley. Part of the avalanching flow overtopped and partly entrained the rock ava-
146   lanche deposit – leaving behind the scour traces observed in the field – and evolved into the channelized de-
147   bris flow which arrived at Bondo a couple of minutes later. The secondary debris flow surges started from the
148   rock avalanche deposit due to melting and infiltration of the remaining ice, and due to backwater effects. This
149   scenario is similar to the theory developed at the WSL Institute for Snow and Avalanche Research (SLF), who
150   also did a first simulation of the rock avalanche (WSL, 2017).

151   Fig. 5 illustrates the conceptual models attempting to explain the key mechanisms involved in the rock avalanche-
152 debris flow transformation.

3   The simulation framework r.avaflow

154 r.avaflow represents a comprehensive GIS-based open source framework which can be applied for the simulation of
155 various types of geomorphic mass flows. In contrast to most other mass flow simulation tools, r.avaflow utilizes a gen-
156 eral two-phase-flow model describing the dynamics of the mixture of solid particles and viscous fluid and the strong
157 interactions between these phases. It further considers erosion and entrainment of surface material along the flow
158 path. These features facilitate the simulation of cascading landslide processes such as the 2017 Piz Cengalo-Bondo
159 event. r.avaflow is outlined in full detail by Mergili et al. (2017). The code, a user manual, and a collection of test da-
160 tasets are available from Mergili (2019). Only those aspects directly relevant for the present work are described in this
161 section.

162 Essentially, the Pudasaini (2012) two-phase flow model is employed for computing the dynamics of mass flows moving
163 from a defined release area (solid and/or fluid heights are assigned to each raster cell) or release hydrograph (at each
164 time step, solid and/or fluid heights are added at a given profile, moving at a given cross-profile velocity) down
165 through a DEM. The spatio-temporal evolution of the flow is approximated through depth-averaged solid and fluid
166 mass and momentum balance equations (Pudasaini, 2012). This system of equations is solved through the TVD-NOC

167 Scheme introduced by Nessyahu and Tadmor (1990), adapting an approach presented by Tai et al. (2002) and Wang et

168 al. (2004). The characteristics of the simulated flow are governed by a set of flow parameters (some of them are shown

169 in the Tables 1 and 2). Compared to the Pudasaini (2012) model, some extensions have been introduced which include

170 (i) ambient drag or air resistance (Kattel et al., 2016; Mergili et al., 2017); and (ii) fluid friction, governing the influ-

171 ence of basal surface roughness on the fluid momentum (Mergili et al., 2018b). Both extensions rely on empirical coef-

172 ficients, C_{AD} for the ambient drag and C_{FF} for the fluid friction. Further, drag and viscosity are computed according to

173 enhanced concepts. Most importantly, the internal friction angle φ and the basal friction angle δ of the solid are scaled

174 with the solid fraction in order to approximate effects of reduced interaction between the solid particles and the basal

175 surface in fluid-rich flows.

176 Entrainment is calculated through an empirical model. In contrast to Mergili et al. (2017), where an empirical en-

177 trainment coefficient is multiplied with the momentum of the flow, here we multiply the entrainment coefficient

178 C_E (s kg⁻¹ m⁻¹) with the kinetic energy of the flow:

179 $$q_{E,s} = C_E |T_s + T_f| \alpha_{s,E}, \; q_{E,f} = C_E |T_s + T_f| (1 - \alpha_{s,E}), \quad (1)$$

180 where $q_{E,s}$ and $q_{E,f}$ (m s⁻¹) are the solid and fluid entrainment rates, T_s and T_f (J) are the kinetic energies of the solid and

181 fluid fractions of the flow, and $\alpha_{s,E}$ is the solid fraction of the entrainable material. Solid and fluid flow heights and

182 momenta, and the change of the basal topography, are updated at each time step (see Mergili et al., 2017 for details).

183 As r.avaflow operates on the basis of GIS raster cells, its output essentially consists of raster maps –for all time steps

184 and for the overall maximum – of solid and fluid flow heights, velocities, pressures, kinetic energies, and entrained

185 heights. In addition, output hydrograph profiles may be defined at which solid and fluid heights, velocities, and dis-

186 charges are provided at each time step.

4 Parameterization of r.avaflow

188 One set of simulations is performed for each of the Scenarios A and B (Fig. 5), considering the process chain from the

189 release of the rock slide-rock fall to the arrival of the first debris flow surge at Bondo. Neither triggering of the event

190 nor subsequent surges or distal debris floods beyond Bondo are considered in this study. Equally, the dust cloud associ-

191 ated to the rock avalanche (WSL, 2017) is not the subject here. Initial sliding of the glacier beneath the rock ava-

192 lanche, as assumed in Scenario B, cannot directly be modelled. That would require a three-phase model, which is be-

193 yond the scope here. Instead, release of the glacier ice and meltwater is assumed in a separate simulation after the rock

194 avalanche has passed over it. We consider this workaround an acceptable approximation of the postulated scenario

195 (Section 6).

196 We use the 2011 swisstopo MNS-DEM, corrected for the rock slide-rock fall scarp and the entrained glacier ice by

197 overlay with the 2017 SfM DSM (Section 2). The maps of release height and maximum entrainable height are derived

198 from the difference between the 2011 swisstopo DTM and the 2017 SfM DSM (Fig. 4; Section 2). The release mass is

199 considered completely solid, whereas the entrained glacier is assumed to contain some solid fraction (coarse till). The

200 glacier ice is assumed to melt immediately on impact and is included in the fluid along with fine till. We note that the

201 fluid phase does not represent pure water, but a mixture of water and fine particles (Table 2). The fraction of the glaci-

202 er allowed to be incorporated in the process chain is empirically optimized (Table 3). Based on the same principle, the

203 maximum depth of entrainment of fluid due to pore pressure overload in Scenario A is set to 25 cm, whereas the max-

204 imum depth of entrainment of the rock avalanche deposit in Scenario B is set to 1 m.

205 The study area is divided into six zones A–F (Fig. 6; Table 1). Each of these zones represents an area with particular

206 surface and flow characteristics, which can be translated into model parameters. Due to the impossibility to directly

207 measure the key parameters in the field (Mergili et al., 2018a, b), the parameters summarized in Table 1 and Table 2

208 are the result of an iterative optimization procedure, where multiple simulations with different parameter sets are

209 performed in order to arrive at one "optimum" simulation for each scenario. It is thereby important to note that we

210 largely derive one single set of optimized parameters, which is valid for both of the scenarios. Optimization criteria are

211 (i) the empirical adequacy of the model results, and (ii) the physical plausibility of the parameters. Thereby, the empir-

212 ical adequacy is quantified through comparison of the results with the documented impact area, the travel times to the

213 output hydrograph profiles O2, O3, and O4 (Fig. 6), and the reported volumes (Amt für Wald und Naturgefahren,

214 2017; Bonanomi and Keiser, 2017; WSL, 2017). The physical plausibility of the model parameters is evaluated on the

215 basis on the parameters suggested by Mergili et al. (2017) and on the findings of Mergili et al. (2018a, b). We note that

216 the values of the basal friction angle (δ), the ambient drag coefficient (C_{AD}), the fluid friction coefficient (C_{FF}), and the

217 entrainment coefficient (C_E) are differentiated between and within the zones (Table 1), whereas global values are de-

218 fined for all the other parameters (Table 2).

219 Durations of $t = 1800$ s are considered for both scenarios. At this point of time, the first debris flow surge has largely

220 passed and left the area of interest, except for some remaining tail of fluid material. Only heights ≥0.25 m are taken

221 into account for the visualization and evaluation of the simulation results. Considering the size of the event, a cell size

222 of 10 m is considered the best compromise between capturing a sufficient level of detail and ensuring an adequate

223 computational efficiency, and is therefore applied for all simulations.

5   Simulation results

5.1   Scenario A – Frontal debris flow surge

226 Fig. 7 illustrates the distribution of the simulated maximum flow heights, maximum entrained heights, and deposition

227 area after $t = 1800$ s, when most of the initial debris flow surge has passed the confluence of the Bondasca stream and

228 the Maira river. The comparison of observed and simulated impact areas results in a critical success index $CSI = 0.568$,

229 a distance to perfect classification $D2PC = 0.149$, and a factor of conservativeness $FoC = 1.523$. These performance in-

230 dicators are derived from the confusion matrix of true positives, true negatives, false positives, and false negatives.

231 They are explained in more detail by Mergili et al. (2018b). Interpreting these values as indicators for a reasonably

232 good correspondence between simulation and observation in terms of impact area, we now consider the dimension of

233 time, focussing on the output hydrographs OH1–OH4 (Fig. 8; see Fig. 6 and Fig. 7 for the location of the correspond-

234 ing hydrograph profiles O1–O4). Most of the rock avalanche passes the profile O1 between $t = 40$ s and $t = 100$ s. OH2

235 (Fig. 8a; located in the upper portion of Val Bondasca) sets on before $t = 140$ s and quickly reaches its peak, with a vol-

236 umetric solid ratio of approx. 34% (maximum 900 m³/s of solid and 1,760 m³/s of fluid discharge). Thereafter, this first

237 surge quickly tails off and then remains at total discharge values below 400 m³/s. The solid flow height, however, re-

238 mains above 2 m until the end of the simulation, whereas the fluid flow height slowly and steadily tails off. Until

239 $t = 1800$ s the profile O2 is passed by a total of 183,000 m³ of solid and 252,000 m³ of fluid material (the fluid repre-

240 senting a mixture of fine mud and water with a density of 1,400 kg m⁻³; see Table 2). The hydrograph profile O3 in

241 Prä, approx. 1 km upstream of Bondo, is characterized by a surge starting before $t = 260$ s and slowly tailing off after-

242 wards. Discharge at the hydrograph OH4 (Fig. 8b; O4 is located at the outlet of the canyon to the debris fan of Bondo)

243 starts before t = 740 s and reaches its peak of solid discharge at $t = 940$ s (89 m³/s). Solid discharge decreases thereafter,

244 whereas the flow becomes fluid-dominated with a fluid peak of 135 m³/s at $t = 1440$ s. The maximum total flow height

245 simulated at O4 is 1.25 m. This site is passed by a total of 49,000 m³ of solid and 108,000 m³ of fluid material, according

246 to the simulation – an overestimate, compared to the documentation (Table 3).

247 Fig. 9 illustrates the travel time and the frontal velocities of the rock avalanche and the initial debris flow. The initial

248 surge reaches the hydrograph profile O3 – located 1 km upstream of Bondo – at $t = 260$ s (Fig. 9a; Fig. 8c). This is in

249 line with the documented arrival of the surge at the nearby monitoring station (Table 3). Also the simulated travel

250 time to the profile O4 corresponds to the – though uncertain – documentation. The initial rock avalanche is character-

251 ized by frontal velocities >25 m/s, whereas the debris flow largely moves at 15–25 m/s. Velocities drop below 15 m/s in

252 the upper part of the Val Bondasca (Zone D), and below 5 m/s in the lower part of the valley (Zone E) (Fig. 9b).

253 **5.2   Scenario B – Debris flow surge by overtopping and entrainment of rock avalanche**

254 Fig. 10 illustrates the distribution of the simulated maximum flow heights, maximum entrained heights, and deposi-

255 tion area after $t = t_0 + 1740$ s, where t_0 is the time between the release of the initial rock avalanche and the mobiliza-

256 tion of the entrained glacier. The simulated impact and deposition areas of the initial rock avalanche are also shown in

257 Fig. 10. However, we now concentrate to the debris flow, triggered by the entrainment of 150,000 m³ of solid material

258 from the rock avalanche deposit. Flow heights – as well as the hydrographs presented in Fig. 8c and d and the tem-

259 poral patterns illustrated in Fig. 11 – only refer to the debris flow developing from the entrained glacier and the en-

260 trained rock avalanche material. The confusion matrix of observed and simulated impact areas reveals partly different

261 patterns of performance than for the Scenario A: $CSI = 0.614$; $D2PC = 0.278$; and $FoC = 0.904$. The lower FoC value

262 and the lower performance in terms of $D2PC$ reflect the missing initial rock avalanche in the simulation results. The

263 output hydrographs OH2 and OH4 differ from the hydrographs obtained through the Scenario A, but also show some

264 similarities (Fig. 8c and d). Most of the flow passes through the hydrograph profile O1 between $t = t_0 + 40$ s and

265 $t_0 + 80$ s, and through O2 between $t = t_0 + 120$ s and $t_0 + 180$ s. The hydrograph OH2 is characterized by a short peak of

266   2,700 m³/s of solid and 3,400 m³/s of fluid, with a volumetric solid fraction of 0.45 and quickly decreasing discharge

267   and solid fraction afterwards (Fig. 8c). In contrast to Scenario A, flow heights drop steadily, with values below 2 m

268   from $t = t_0 + 920$ s onwards. The hydrograph OH3 is characterized by a surge starting before $t = t_0 + 260$ s. Discharge at

269   the hydrograph OH4 (Fig. 8d) starts at $t = t_0 + 740$ s, and the solid peak of 160 m³/s is simulated approx. at

270    $t = t_0 + 1080$ s. The delay of the peak of fluid discharge is less pronounced when compared to Scenario A (265 m³/s at

271    $t = t_0 + 1180$ s). Profile O4 is passed by a total of 53,000 m³ of solid and 143,000 m³ of fluid material. The volumetric

272   solid fraction drops from above 0.70 at the onset of the hydrograph to almost zero (pure fluid) at the end. The maxi-

273   mum total flow height at O4 is 3.7 m.

274   Fig. 11 illustrates the travel times and the frontal velocities of the rock avalanche and the initial debris flow. Assuming

275   that t_0 is in the range of some tens of seconds, the time of arrival of the surge at O3 is in line with the documentation

276   also for the Scenario B (Fig. 11a; Table 3). The frontal velocity patterns along Val Bondasca are very much in line with

277   those derived in the Scenario A (Fig. 11b). However, the scenarios differ among themselves in terms of the more pro-

278   nounced, but shorter peaks of the hydrographs in Scenario B (Fig. 8). This pattern is a consequence of the more sharp-

279   ly defined debris flow surge. In Scenario A, the front of the rock avalanche deposit constantly "leaks" into Val Bon-

280   dasca, providing supply for the debris flow also at later stages. In Scenario B, entrainment of the rock avalanche depos-

281   it occurs relatively quickly, without material supply afterwards. This type of behaviour is strongly coupled to the value

282   of C_E and the allowed height of entrainment chosen for the rock avalanche deposit.

6 Discussion

284   Our simulation results reveal a reasonable degree of empirical adequacy and physical plausibility with regard to most

285   of the reference observations. Having said that, we have also identified some important limitations which are now

286   discussed in more detail. First of all, we are not able to decide on the more realistic of the two Scenarios A and B. In

287   general, the melting and mobilization of glacier ice upon rock slide-rock fall impact is hard to quantify from straight-

288   forward calculations of energy transformation, as Huggel et al. (2005) have demonstrated on the example of the 2002

289   Kolka-Karmadon event. In the present work, the assumed amount of melting (approx. half of the glacier ice) leading to

290   the empirically most adequate results corresponds well to the findings of WSL (2017), indicating a reasonable degree

291   of plausibility. It remains equally difficult to quantify the amount of water injected into the rock avalanche by over-

292   load of the sediments and the resulting pore pressure rise.

293   We note that with the approach chosen we are not able (i) to adequately simulate the transition from solid to fluid

294   material; and (ii) to consider rock and ice separately with different material properties, which would require a three-

295   phase model, not within the scope here. Therefore, entrained ice is considered viscous fluid from the beginning. A

296   physically better founded representation of the initial phase of the event would require an extension of the flow model

297   employed. Such an extension could build on the rock-ice avalanche model introduced by Pudasaini and Krautblatter

298   (2014). Also the vertical patterns of the situation illustrated in Fig. 4 cannot be modelled with the present approach,

299   which (i) does not consider melting of ice; and (ii) only allows one entrainable layer at each pixel. The assumption of
300   fluid behaviour of glacier ice therefore represents a necessary simplification which is supported by observations
301   (Fig. 3b), but neglects the likely presence of remaining ice in the basal part of the eroded glacier, which melted later
302   and so contributed to the successive debris flow surges.

303   The initial rock slide-rock fall and the rock avalanche are simulated in a plausible way, at least with regard to the dep-
304   osition area. Whereas the simulated deposition area is clearly defined in Scenario B, this is to a lesser extent the case in
305   Scenario A, where the front of the rock avalanche directly transforms into a debris flow. Both scenarios seem to over-
306   estimate the time between release and deposition, compared to the seismic signals recorded – an issue also reported by
307   WSL (2017) for their simulation. We observe a relatively gradual deceleration of the simulated avalanche, without
308   clearly defined stopping and note that also in the Scenario B, there is some diffusion after the considered time of 120 s,
309   so that the definition of the simulated deposit is somehow arbitrary. The elaboration of well-suited stopping criteria,
310   going beyond the very simple approach introduced by Mergili et al. (2017), remains a task for the future. However, as
311   the rock avalanche has already been successfully back-calculated by WSL (2017), we focus on the first debris flow
312   surge: the simulation input is optimized towards the back-calculation of the debris flow volumes entering the valley at
313   the hydrograph profile O2 (Table 3). The travel times to the hydrograph profiles O3 and O4 are reproduced in a plau-
314   sible way in both scenarios, and so are the impact areas (Figs. 7 and 10). Exceedance of the lateral limits in the lower
315   zones is attributed to an overestimate of the debris flow volumes there, and to numerical issues related to the narrow
316   gorge. The solid ratio of the debris flow in the simulations appears realistic, ranging around 45% in the early stage of
317   the debris flow, and around 30% in the final stage. This means that solid material tends to stop in the transit area ra-
318   ther than fluid material, as it can be expected. Nevertheless, the correct simulation of the deposition of debris flow
319   material along Val Bondasca remains a major challenge (Table 3). Even though a considerable amount of effort was put
320   in reproducing the much lower volumes reported in the vicinity of O4, the simulations result in an overestimate of the
321   volumes passing through this hydrograph profile. This is most likely a consequence of the failure of r.avaflow to ade-
322   quately reproduce the deposition pattern in the zones D and E. Whereas some material remains there at the end of the
323   simulation, and even more material is lost due to numerical diffusion, more work is necessary to appropriately under-
324   stand the mechanisms of deposition in viscous debris flows (Pudasaini and Fischer, 2016b). Part of the discrepancy,
325   however, might be explained by the fact that part of the fluid material – which does not only consist of pure water,
326   but of a mixture of water and fine mud – left the area of interest in downstream direction and was therefore not in-
327   cluded in the reference measurements.

328   The simulation results are strongly influenced by the initial conditions and the model parameters. Parameterization of
329   both scenarios is complex and highly uncertain, particularly in terms of optimizing the volumes of entrained till and
330   glacial meltwater, and injected pore water. In general, the parameter sets optimized to yield empirically adequate re-
331   sults are physically plausible, in contrast to Mergili et al. (2018b) who had to set the basal friction angle in a certain
332   zone to a negligible value in order to reproduce the observed overtopping of a more than 100 m high ridge (1970
333   Huascarán landslide). In contrast, reproducing the travel times to O4 in the present study requires the assumption of a

Natural Hazards
and Earth System
Sciences
Discussions

334 low mobility of the flow in Zone E. This is achieved by increasing the friction (Table 1), accounting for the narrow

335 flow channel, i.e. the interaction of the flow with the channel walls, which is not directly accounted for in r.avaflow.

336 Still, the high values of δ given in Table 1 are not directly applied, as they scale with the fluid content. This type of

337 weighting has to be further scrutinized. We emphasize that also reasonable parameter sets are not necessarily true, as

338 the large number of parameters involved (Tables 1 and 2) creates a lot of space for equifinality issues (Beven et al.,

339 1996).

340 We have further shown that the classical evaluation of empirical adequacy, by comparing observed and simulated

341 impact areas, is not enough in the case of complex mass flows: travel times, hydrographs, and volumes involved can

342 provide important insight in addition to the classical quantitative performance indicators used, for example, in land-

343 slide susceptibility modelling (Formetta et al., 2015). Further, the delineation of the observed impact area is uncertain

344 as the boundary of the event is not clearly defined particularly in Zone C.

7 Conclusions

346 Both of the investigated Scenarios A and B lead to empirically reasonably adequate results, when back calculated with

347 r.avaflow using physically plausible model parameters. Based on the simulations performed in the present study, final

348 conclusions on the more likely of the mechanisms sketched in Fig. 5 can therefore not be drawn purely based on the

349 simulations. The observed jet of glacial meltwater (Fig. 3b) points towards Scenario A. The observed scouring of the

350 rock avalanche deposit, in contrast, rather points towards Scenario B, but could also be associated to subsequent debris

351 flow surges. Open questions include at least (i) the interaction between the initial rock slide-rock fall and the glacier;

352 (ii) flow transformations in the lower portion of Zone C (Fig. 6), leading to the first debris flow surge; and (iii) the

353 mechanisms of deposition of 90% of the debris flow material along the flow channel in the Val Bondasca. Further re-

354 search is therefore urgently needed to shed more light on this extraordinary landslide cascade in the Swiss Alps. In

355 addition, improved simulation concepts are needed to better capture the dynamics of complex landslides in glacierized

356 environments: such would particularly have to include three-phase models, where ice – and melting of ice – are con-

357 sidered in a more explicit way.

Acknowledgements

References

369   Alean, J.: Ice avalanches: some empirical information about their formation and reach, J. Glaciol., 31(109), 324–333,

370   https://doi.org/10.3189/S0022143000006663, 1985.

371   Amann, F., Kos, A., Phillips, M., and Kenner, R.: The Piz Cengalo Bergsturz and subsequent debris flows, Geophys.

372   Res. Abstr., 20, 14700, 2018.

373   Amt   für   Wald   und   Naturgefahren: Bondo: Chronologie   der   Ereignisse,   2 pp.,

374   https://www.gr.ch/DE/institutionen/verwaltung/bvfd/awn/dokumentenliste_afw/20170828_Chronologie_Bondo_2017

375   _12_13_dt.pdf, accessed on 31 May 2019.

376   Beven, K.: Equifinality and Uncertainty in Geomorphological Modelling, in: The Scientific Nature of Geomorphology:

377   Proceedings of the 27th Binghamton Symposium in Geomorphology, 27-29 September 1996, John Wiley & Sons, 289–

378   313, 1996.

379   Bonanomi, Y., and Keiser, M.: Bericht zum aktuellen Bergsturz am Piz Cengalo 2017, Bergeller Alpen im Engadin, 19.

380   Geoforum Umhausen, 19.–20. Oktober 2017, 55–60, 2017.

381   Christen, M., Kowalski, J., and Bartelt, P.: RAMMS: Numerical simulation of dense snow avalanches in three-

382   dimensional terrain, Cold Reg. Sci. Technol., 63, 1–14, https://doi.org/10.1016/j.coldregions.2010.04.005, 2010.

383   De Blasio, F. V., and Crosta, G. B.: Extremely Energetic Rockfalls: Some preliminary estimates, in: Landslides and En-

384   gineered Slopes. Experience, Theory and Practice, 759–764, CRC Press, 2016.

385   Demmel, S.: Water Balance in Val Bondasca. Initial hydrological conditions for debris flows triggered by the 2017 rock

386   avalanche at Pizzo Cengalo. Master Thesis, ETH Zurich, 50 pp., 2019.

387   Evans, S. G., Bishop, N.F., Fidel Smoll, L., Valderrama Murillo, P., Delaney, K.B., and Oliver-Smith, A.: A re-

388   examination of the mechanism and human impact of catastrophic mass flows originating on Nevado Huascarán, Cor-

389   dillera Blanca, Peru in 1962 and 1970, Eng. Geol., 108, 96–118, https://doi.org/10.1016/j.enggeo.2009.06.020, 2009.

390   Evans, S. G., and Delaney, K. B.: Catastrophic mass flows in the mountain glacial environment, in: Snow and Ice-

391   related Hazards, Risks and Disasters, edited by: Haeberli, W., and Whiteman, C., Elsevier, 563–606,

392   https://doi.org/10.1016/B978-0-12-394849-6.00016-0, 2014.

393   Fischer, J.-T., Kowalski, J., and Pudasaini, S. P.: Topographic curvature effects in applied avalanche modeling, Cold

394   Reg. Sci. Technol., 74, 21–30, https://doi.org/10.1016/j.coldregions.2012.01.005, 2012.

395   Fischer, J.-T., Kofler, A., Fellin, W., Granig, M., and Kleemayr, K.: Multivariate parameter optimization for computa-
396   tional snow avalanche simulation in 3d terrain, J. Glaciol., 61(229), 875–888, https://doi.org/10.3189/2015JoG14J168,
397   2015.

398   Formetta, G., Capparelli, G., and Versace, P.: Evaluating performances of simplified physically based models for land-
399   slide susceptibility, Hydrol. Earth Syst. Sci. Discuss., 12, 13217–13256, https://doi.org/10.5194/hessd-19-1-2015, 2015.

400   Gruber, S., and Haeberli, W.: Permafrost in steep bedrock slopes and its temperature-related destabilization following
401   climate change, J. Geophys. Res. Earth Surf., 112, F02S18, http://dx.doi:10.1029/2006JF000547, 2007.

402   Haeberli, W.: Construction, environmental problems and natural hazards in periglacial mountain belts, Permafrost
403   Periglacial Process., 3(2), 111–124, https://doi.org/10.1002/ppp.3430030208, 1992.

404   Haeberli, W.: Mountain permafrost—research frontiers and a special long-term challenge, Cold Reg. Sci. Technol., 96,
405   71–76, https://doi.org/10.1016/j.coldregions.2013.02.004, 2013.

406   Haeberli, W., and Whiteman, C. (Eds.): Snow and Ice-related Hazards, Risks and Disasters, Elsevier,
407   https://doi.org/10.1016/B978-0-12-394849-6.00001-9, 2014.

408   Haeberli, W., Wegmann, M., and Von der Muehll, D.: Slope stability problems related to glacier shrinkage and perma-
409   frost degradation in the Alps, Eclogae Geologicae Helveticae, 90, 407–414, 1997.

410   Haeberli, W., Schaub, Y., and Huggel, C.: Increasing risks related to landslides from degrading permafrost into new
411   lakes   in   de-glaciating   mountain   ranges,   Geomorphology,   293(B),   405–417,
412   https://doi.org/10.1016/j.geomorph.2016.02.009, 2017.

413   Harris, C., Arenson, L. U., Christiansen, H. H., Etzelmüller, B., Frauenfelder, R., Gruber, S., Haeberli, W., Hauck., C.,
414   Hölzle, M., Humlum, O., Isaksen, K., Kääb, A., Kern-Lütschg, M. A., Lehning, M., Matsuoka, N., Murton, J. B., Nötzli,
415   J., Phillips, M., Ross, N., Seppälä, M., Springman, S. M., and Vonder Mühll, D.: Permafrost and climate in Europe:
416   Monitoring and modelling thermal, geomorphological and geotechnical responses, Earth-Sci. Rev., 92, 117–171,
417   https://doi.org/10.1016/j.earscirev.2008.12.002, 2009.

418   Huggel, C., Kääb, A., Haeberli, W., and Krummenacher, B.: Regional-scale GIS-models for assessment of hazards from
419   glacier lake outbursts: evaluation and application in the Swiss Alps, Nat. Hazards Earth Syst. Sci., 3, 647–662,
420   https://doi.org/10.5194/nhess-3-647-2003, 2003.

421   Huggel, C., Zgraggen-Oswald, S., Haeberli, W., Kääb, A., Polkvoj, A., Galushkin, I., and Evans, S.G.: The 2002 rock/ice
422   avalanche at Kolka/Karmadon, Russian Caucasus: assessment of extraordinary avalanche formation and mobility, and
423   application of QuickBird satellite imagery, Nat. Hazards Earth Syst. Sci., 5, 173–187, https://doi.org/10.5194/nhess-5-
424   173-2005, 2005.

Natural Hazards
and Earth System
Sciences
Discussions

425 Huggel, C., Salzmann, N., Allen, S., Caplan-Auerbach, J., Fischer, L., Haeberli, W., Larsen, C., Schneider, D., and Wes-
426 sels, R.: Recent and future warm extreme events and high-mountain slope stability, Philos. Trans. R. Soc. A, 368,
427 2435–2459, https://doi.org/10.1098/rsta.2010.0078, 2010.

428 Huggel, C., Clague, J. J., and Korup, O.: Is climate change responsible for changing landslide activity in high moun-
429 tains?, Earth Surf. Process. Landf., 37, 77–91, https://doi.org/10.1002/esp.2223, 2012.

430 Iverson, R. M.: The physics of debris flows, Rev. Geophys., 35, 245–296, https://doi.org/10.1029/97RG00426, 1997.

431 Kattel. P , Khattri, K. B., Pokhrel, P. R., Kafle, J., Tuladhar, B. M., and Pudasaini, S. P.: Simulating glacial lake outburst
432 floods with a two-phase mass flow model, Ann. Glaciol., 57(71), 349–358, https://doi.org/10.3189/2016AoG71A039,
433 2016.

434 Krautblatter, M., Funk, D., and Günzel, F. K.: Why permafrost rocks become unstable: a rock–ice-mechanical model
435 in time and space, Earth Surf. Process. Landf., 38, 876–887, https://doi.org/10.1002/esp.3374, 2013.

436 McDougall, S., and Hungr, O.: A Model for the Analysis of Rapid Landslide Motion across Three-Dimensional Terrain,
437 Can. Geotech. J., 41, 1084–1097, https://doi.org/10.1139/t04-052, 2004.

438 Mergili, M.: r.avaflow – The open source mass flow simulation model, https://www.avaflow.org/, last access: 7 July
439 2019.

440 Mergili, M., Fischer, J.-T., Krenn, J., and Pudasaini, S. P.: r.avaflow v1, an advanced open source computational
441 framework for the propagation and interaction of two-phase mass flows, Geosci. Model Dev., 10, 553–569,
442 https://doi.org/10.5194/gmd-10-553-2017, 2017.

443 Mergili, M., Emmer, A., Juřicová, A., Cochachin, A., Fischer, J.-T., Huggel, C., and Pudasaini, S.P.: How well can we
444 simulate complex hydro-geomorphic process chains? The 2012 multi-lake outburst flood in the Santa Cruz Valley
445 (Cordillera Blanca, Perú), Earth Surf. Process. Landf., 43(7), 1373–1389, https://doi.org/10.1002/esp.4318, 2018a.

446 Mergili, M., Frank, B., Fischer, J.-T., Huggel, C., and Pudasaini, S. P.: Computational experiments on the 1962 and
447 1970 landslide events at Huascarán (Peru) with r.avaflow: Lessons learned for predictive mass flow simulations, Geo-
448 morphology, 322, 15–28, https://doi.org/10.1016/j.geomorph.2018.08.032, 2018b.

449 Nessyahu, H.., and Tadmor, E.: Non-oscillatory central differencing for hyperbolic conservation laws, J. Comput.
450 Phys., 87, 408–463, https://doi.org/10.1016/0021-9991(90)90260-8, 1990.

451 Noetzli, J., Huggel, C., Hoelzle, M., and Haeberli, W.: GIS-based modelling of rock-ice avalanches from Alpine perma-
452 frost areas, Comput. Geosci., 10, 161–178, https://doi.org/10.1007/s10596-005-9017-z, 2006.

453 Pitman, E.B., and Le, L.: A two-fluid model for avalanche and debris flows. Philos. Trans. R. Soc. A, 363, 1573–1601,
454 https://doi.org/10.1098/rsta.2005.1596, 2005.

455 Pudasaini, S. P.: A general two-phase debris flow model, J. Geophys. Res. Earth Surf., 117, F03010,
456 https://doi.org/10.1029/2011JF002186, 2012.

457   Pudasaini, S. P.: A full description of generalized drag in mixture mass flows, Phys. Fluids, submitted manuscript,
458   2019.

459   Pudasaini, S. P., and Krautblatter, M.: A two-phase mechanical model for rock-ice avalanches, J. Geophys. Res. Earth
460   Surf., 119, doi:10.1002/2014JF003183, 2014.

461   Pudasaini, S. P., and Fischer, J.-T.: A mechanical model for phase-separation in debris flow, arXiv:1610.03649, 2016a.

462   Pudasaini, S.P., and Fischer, J.-T.: A mechanical erosion model for two-phase mass flows, arXiv:1610.01806, 2016b.

463   Preh, A., and Sausgruber, J. T.: The Extraordinary Rock-Snow Avalanche of Alpl, Tyrol, Austria. Is it Possible to Pre-
464   dict the Runout by Means of Single-phase Voellmy- or Coulomb-Type Models?, in: Engineering Geology for Society
465   and Territory–Volume 2, edited by: Lollino, G. et al., Springer, Cham, https://doi.org/10.1007/978-3-319-09057-3_338,
466   2015.

467   Ravanel, L., and Deline, P.: Climate influence on rockfalls in high-Alpine steep rockwalls: the North side of the Ai-
468   guilles de Chamonix (Mont Blanc massif) since the end of the Little Ice Age, Holocene, 21, 357–365,
469   https://doi.org/10.1177/0959683610374887, 2011.

470   Saltelli, A., and Annoni, P.: How to avoid a perfunctory sensitivity analysis, Environ. Model. Softw., 25, 1508–1517,
471   https://doi.org/10.1016/j.envsoft.2010.04.012, 2010.

472   Savage, S. B., and Hutter, K.: The motion of a finite mass of granular material down a rough incline, J. Fluid Mech.,
473   199, 177–215, https://doi.org/10.1017/S0022112089000340, 1989.

474   Schneider, D., Huggel, C., Cochachin, A., Guillén, S., and García, J.: Mapping hazards from glacier lake outburst floods
475   based on modelling of process cascades at Lake 513, Carhuaz, Peru, Adv. Geosci., 35, 145–155,
476   https://doi.org/10.5194/adgeo-35-145-2014, 2014.

477   Somos-Valenzuela, M. A., Chisolm, R. E., Rivas, D. S., Portocarrero, C., and McKinney, D. C.: Modeling a glacial lake
478   outburst flood process chain: the case of Lake Palcacocha and Huaraz, Peru, Hydrol. Earth Syst. Sci., 20, 2519–2543,
479   https://doi.org/10.5194/hess-20-2519-2016, 2016.

480   Steinacher, R., Kuster, C., Buchli, C., and Meier, L.: The Pizzo Cengalo and Val Bondasca events: From early warnings
481   to immediate alarms, Geophys. Res. Abstr. 20, 17536, 2018.

482   Tai, Y. C., Noelle, S., Gray, J. M. N. T., and Hutter, K.: Shock-capturing and front-tracking methods for granular ava-
483   lanches, J. Comput. Phys., 175(1), 269–301, https://doi.org/10.1006/jcph.2001.6946, 2002.

484   VAW: Vadrec dal Cengal Ost: Veränderungen in Vergangenheit und Zukunft. Laboratory of Hydraulics, Hydrology
485   and   Glaciology   of   the   Swiss   Federal   Institute   of   Technology   Zurich,   17   pp.,
486   https://www.gr.ch/DE/institutionen/verwaltung/bvfd/awn/dokumentenliste_afw/Cengalo%20Gletscherentwicklung%
487   20ETH_2nov_final.pdf, accessed on 31 May 2019, 2017.

488   Voellmy, A.: Über die Zerstörungskraft von Lawinen, Schweizerische Bauzeitung, 73, 159–162, 212–217, 246–249,

489   280–285, 1955.

490   Walter, F., Wenner, M., and Amann, F.: Seismic Analysis of the August 2017 Landslide on Piz Cengalo (Switzerland),

491   Geophys. Res. Abstr., 20, 3163-1, 2018.

492   Walter, F., Amann, F., Kos, A., Kenner, R., Phillips, M., de Preux, A., Huss, M., Tognacca, C., Clinton, J., Diehl, T., and

493   Bonanomi, Y.: Direct observations of a three million cubic meter rock-slope collapse with almost immediate initiation

494   of ensuing debris flows, Earth Planet. Sci. Lett., submitted manuscript, 2019.

495   Wang, Y., Hutter, K., and Pudasaini, S. P.: The Savage-Hutter theory: A system of partial differential equations for

496   avalanche flows of snow, debris, and mud, ZAMM – J. Appl. Math. Mech., 84(8), 507–527,

497   https://doi.org/10.1002/zamm.200310123, 2004.

498   Worni, R., Huggel, C., Clague, J. J., Schaub, Y., and Stoffel, M.: Coupling glacial lake impact, dam breach, and flood

499   processes: A modeling perspective, Geomorphology, 224, 161–176, https://doi.org/10.1016/j.geomorph.2014.06.031,

500   2014.

501   WSL.: SLF Gutachten G2017.20: Modellierung des Cengalo Bergsturzes mit verschiedenen Rahmenbedingungen,

502   Bondo,   GR.   WSL-Institut   für   Schnee-   und   Lawinenforschung   SLF,   69 pp.,

503   https://www.gr.ch/DE/institutionen/verwaltung/bvfd/awn/dokumentenliste_afw/SLF_G2017_20_Modellierung_Cenga

504   lo_Bergsturz_030418_A.pdf, accessed on 31 May 2019, 2017.

505

Tables

Table 1. Descriptions and optimized parameter values for each of the zones A–F (Fig. 6). The names of the model parameters are given in the text and in Table 2. The values provided in Table 2 are assigned to those parameters not shown. (A) and (B) refer to the corresponding scenarios.

Zone	Description	Model parameters	Initial conditions
A	Rock zone – NE face of Piz Cengalo with rock slide-rock fall release area	$\delta = 20°$ (A)[1] $\delta = 15°$ (B)[2] $C_{AD} = 0.2$	Release volume: 3.46 million m³, 100 % solid[3]
B	Glacier zone – Cirque glacier beneath zone A, entrainment of glacier ice[1]	$\delta = 20°$ (A) $\delta = 15°$ (B) $C_E = 10^{-6.5}$	Entrainment of glacier ice and till (Table 3)[4]
C	Slope zone – steep, partly debris-covered glacier forefield leading down to the Val Bondasca	$\delta = 20°$ (A) $\delta = 15°$ (B) $C_E = 10^{-6.5}$ (A) $C_E = 10^{-8.0}$ (B)	Entrainment of injected water in Scenario A Entrainment of rock avalanche deposit in Scenario B
D	Upper Val Bondasca zone – clearly defined flow channel becoming narrower in downstream direction	$\delta = 20\text{-}45°$	No entrainment allowed, increasing friction
E	Lower Val Bondasca zone – narrow gorge	$\delta = 45°$ $C_{FF} = 0.5$	No entrainment allowed, high friction due to lateral confinement
F	Bondo zone – deposition of the debris flow on the cone of Bondo	$\delta = 20°$	No entrainment allowed

[1] Note that in all zones and in both of the scenarios A and B, δ is assumed to scale linearly with the solid fraction. This means that the values given only apply in case of 100% solid.

[2] This only applies to the initial landslide, which is assumed completely dry in Scenario B. Due to the scaling of δ with the solid fraction, a lower basal friction is required to obtain results similar to Scenario A, where the initial landslide contains some fluid. The same values of δ as for Scenario A are applied for the debris flow in Scenario B throughout all zones.

[3] This volume is derived from our own reconstruction (Fig. 4). In contrast, WSL (2017) gives 3.1 million m³, and Amann et al. (2018) 3.15 million m³.

[4] In Scenario B, the glacier is not directly entrained, but instead released behind the rock avalanche. In both scenarios, ice is considered to melt immediately on impact and included in the viscous fluid fraction. See text for more detailed explanations.

Natural Hazards
and Earth System
Sciences
Discussions

Open Access

EGU

522   Table 2. Model parameters used for the simulations.

Symbol	Parameter	Unit	Value
ρ_S	Solid material density (grain density)	kg m^{-3}	2,700
ρ_F	Fluid material density	kg m^{-3}	1,400[1]
φ	Internal friction angle	Degree	27[2]
δ	Basal friction angle	Degree	Table 1
v	Kinematic viscosity of the fluid	m² s^{-1}	10
τ_Y	Yield strength of the fluid	Pa	10
C_{AD}	Ambient drag coefficient	–	0.04 (exceptions in Table 1)
C_{FF}	Fluid friction coefficient		0.0 (exceptions in Table 1)
C_E	Entrainment coefficient	–	Table 1

523   [1] Fluid is here considered as a mixture of water and fine particles. This explains the higher density, compared to pure
524   water.

525   [2] The internal friction angle φ always has to be larger than or equal to the basal friction angle δ. Therefore, in case of
526    $\delta > \varphi$, φ is increased accordingly.

527

528 Table 3. Selected output parameters of the simulations for the Scenarios A and B compared to the observed or docu-
529 mented parameter values. S = solid; F = fluid; fractions are expressed in terms of volume; t_0 = time from the initial re-
530 lease to the release of the first debris flow surge. Reference values are extracted from Amt für Wald und Naturgefah-
531 ren (2017a), Bonanomi and Keiser (2017), and WSL (2017). *** = empirically adequate; ** = empirically partly adequate;
532 * = empirically inadequate.

Parameter	Documenta-tion/Observation	Scenario A	Scenario B
Entrained ice (m³)	600,000[1]	–	–
Entrained S (m³)	–	60,000	60,000[2]
Entrained F (m³)	–	300,000	240,000
Duration of initial landslide	60–90[3]	100–120**	100–120**
Travel time to O2 (s)	90–120[4]	140**	t_0+140**
Travel time to O3 (s)	210–300[5]	260***	t_0+260***
Travel time to O4 (s)	630–1020[6]	740***	t_0+740***
Debris flow volume at O2 (m³)	540,000	440,000*** (42% S***)	400,000*** (45% S***)
Debris flow volume at O4 (m³)	50,000	160,000* (31% S***)	200,000* (27% S***)

533 [1] Not all the material entrained from the glacier was relevant for the first debris flow surge (Fig. 5), therefore lower
534 volumes of entrained S (coarse till, in Scenario B also rock avalanche deposit) and F (molten ice and fine till, in Scenar-
535 io A also pore water) yield the empirically most adequate results. The F volumes originating from the glacier in the
536 simulations represent approx. half of the water equivalent of the entrained ice, corresponding well to the findings of
537 WSL (2017).

538 [2] This value does not include the 140,000 m³ of solid material remobilized through entrainment from the rock ava-
539 lanche deposit in Scenario B.

540 [3] WSL (2017) states that the rock avalanche came to rest approx. 60 s after release, whereas the seismic signals ceased
541 90 s after release.

542 [4] A certain time (here, we assume a maximum of 30 s) has to be allowed for the initial debris flow surge to reach O2,
543 located slightly downstream of the front of the rock avalanche deposit.

544 [5] WSL (2017) gives a travel time of 3.5 minutes to Prä, roughly corresponding to the location of O3. It remains unclear
545 whether this number refers to the release of the initial rock slide-rock fall or (more likely) to the start of the first de-
546 bris flow surge. Bonanomi and Keiser (2017) give a travel time of roughly four minutes between the initial release and
547 the arrival of the first surge at the sensor of Prä.

548 [6] Amt für Wald und Naturgefahren (2017) gives a time span of 17 minutes between the release of the initial rock
549 slide-rock fall and the arrival of the first debris flow surge at the "bridge" in Bondo. However, it is not indicated to
550 which bridge this number refers. WSL (2017), in contrast, give a travel time of 7–8 minutes from Prä to the "old
551 bridge" in Bondo, which, in sum, results in a shorter total travel time as indicated in Amt für Wald und Naturgefahren
552 (2017). Depending on the bridge, the reference location for these numbers might be downstream from O4.
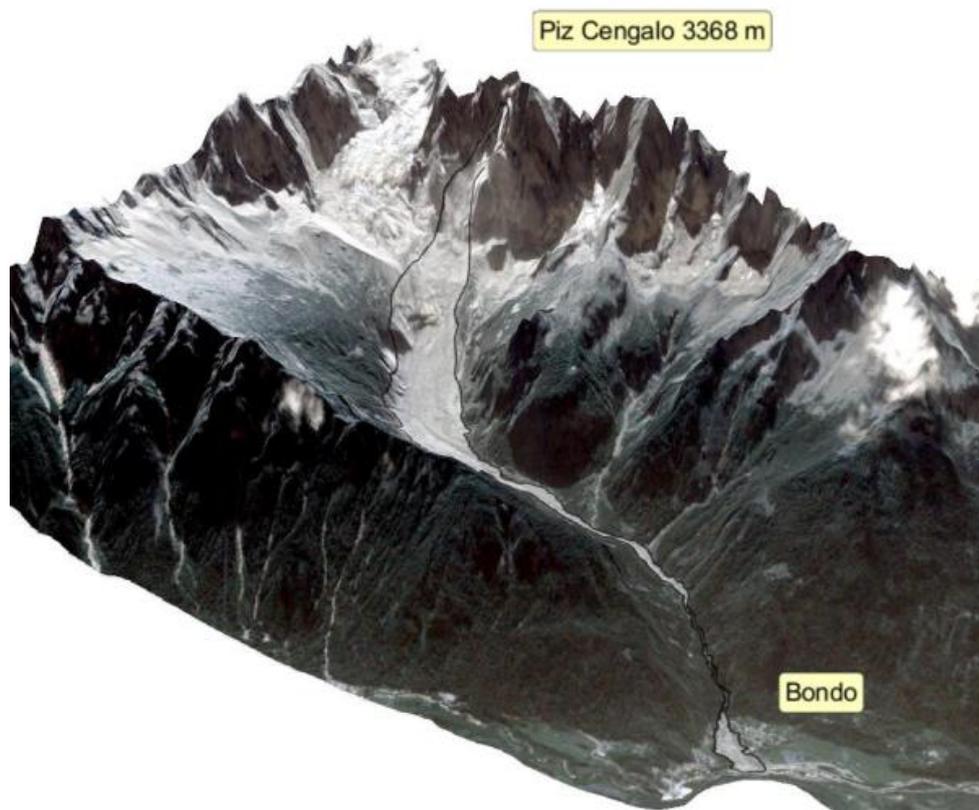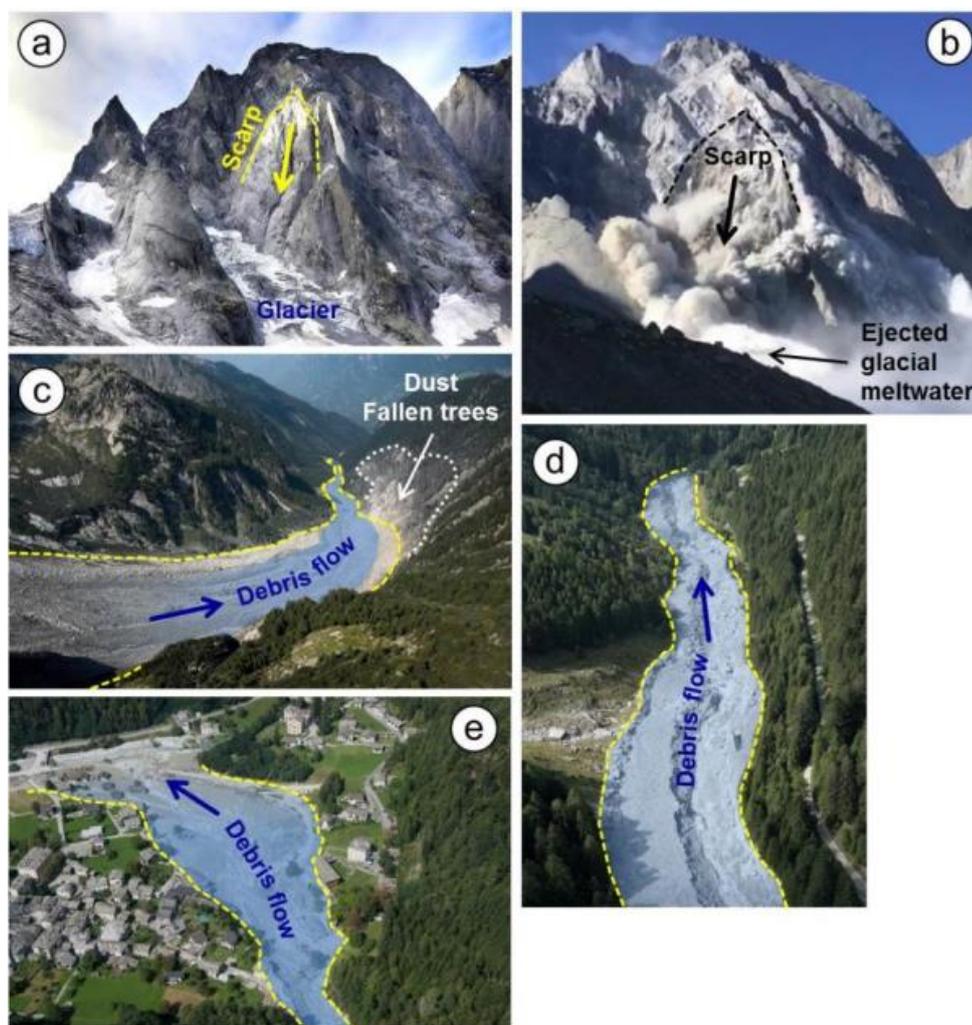
553

554 **Figures**
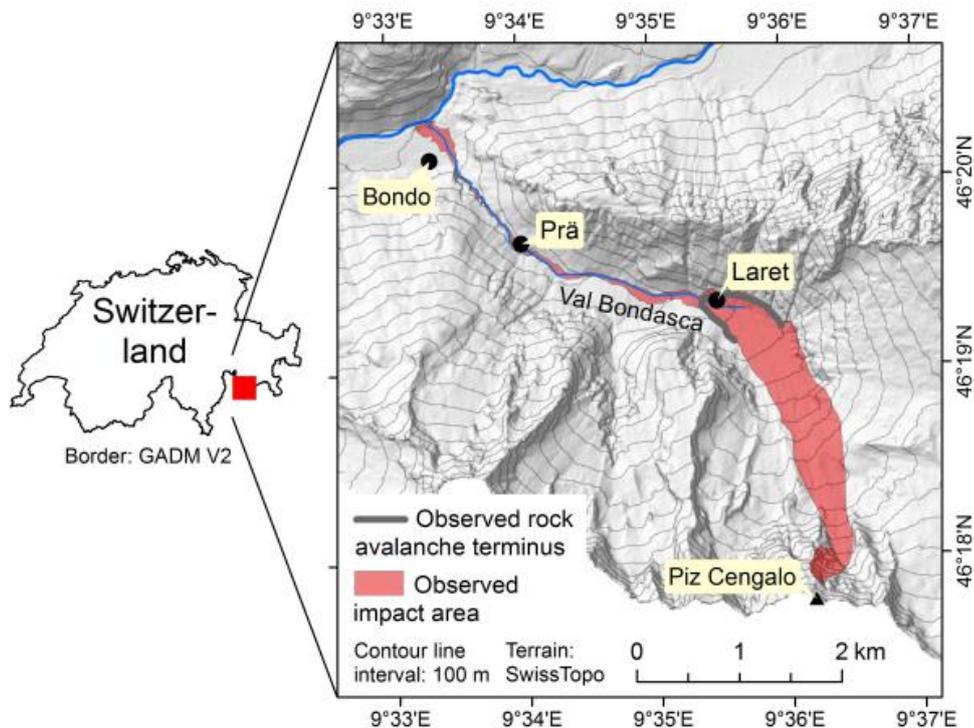
555
556 Figure 1. Study area with the impact area of the 2017 Piz Cengalo-Bondo landslide cascade. The observed rock ava-
557 lanche terminus was derived from WSL (2017).

558

559
560 Figure 2. Oblique view of the impact area of the event, orthophoto draped over the 2011 DTM. Data sources: swis-
561 stopo.

562

Figure 3. The 2017 Piz Cengalo-Bondo landslide cascade. (a) Scarp area on 20 September 2014. (b) Scarp area on 23 September 2017 at 9:30, 20 s after release, frame of a video taken from the Capanna di Sciora. Note the fountain of water and/or crushed ice at the front of the avalanche, most likely representing meltwater from the impacted glacier. (c) Upper part of the Val Bondasca, where the channelized debris flow developed. Note the zone of dust and pressure-induced damages to trees on the right side of the valley. (d) Traces of the debris flows in the Val Bondasca. (e) The debris cone of Bondo after the event. Image sources: Daniele Porro (a), Diego Salasc (b), VBS swisstopo Flugdienst (c)–(e).
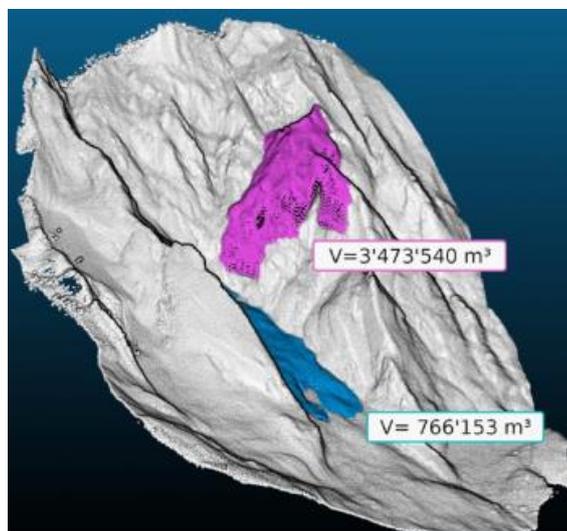
572
573 Figure 4. Reconstruction of the released rock volume and the entrained glacier volume in the 2017 Piz Cengalo-Bondo
574 landslide cascade. Note that the glacier volume shown is neither corrected for entrainment related to the 2011 event,
575 nor for glacier retreat in the period 2011–2017.

576
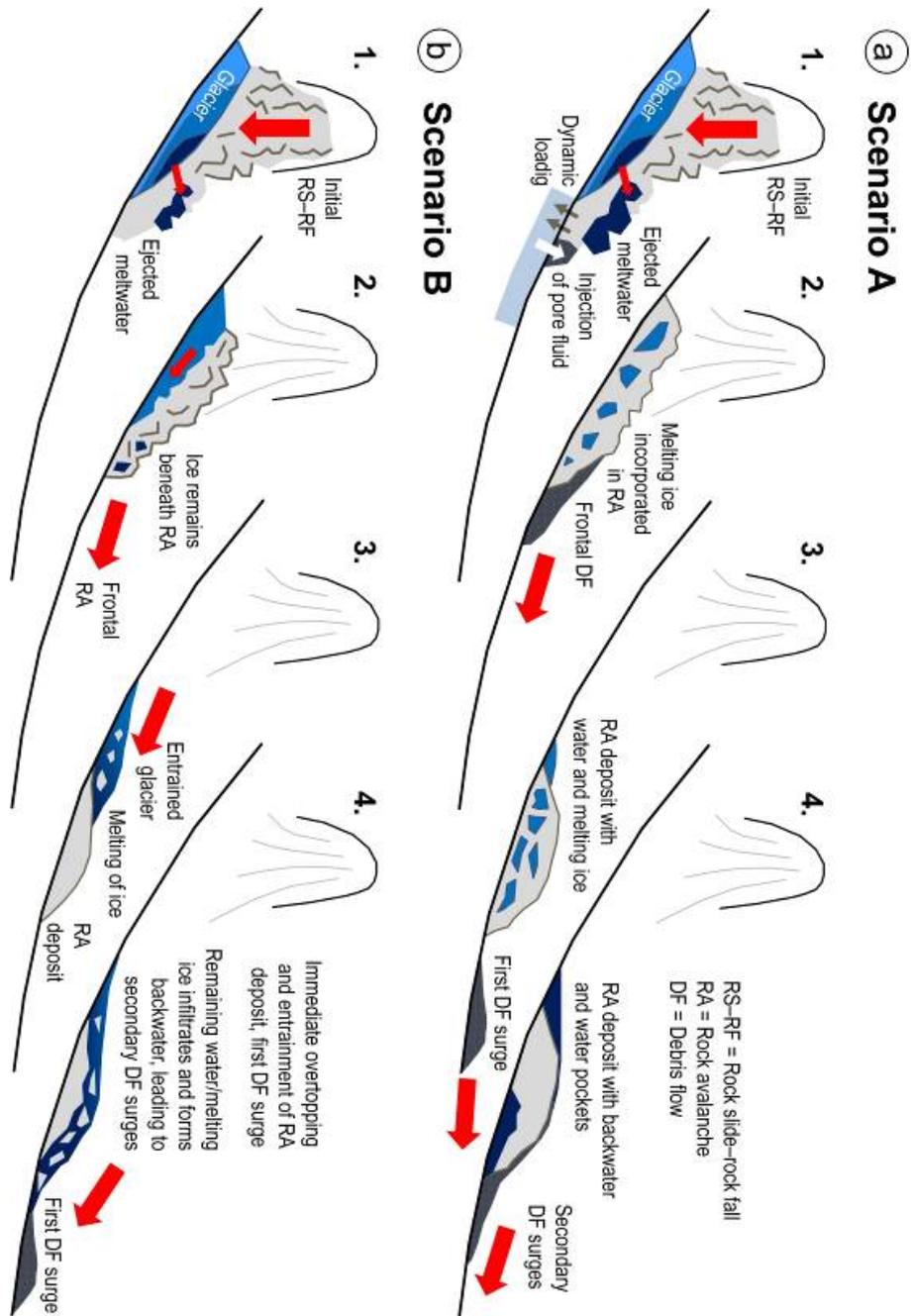
577
578 Figure 5. Qualitative conceptual models of the rock avalanche-debris flow transformation. (a) Scenario A; (b) Scenario
579 B. See text for the detailed description of the two scenarios.

580
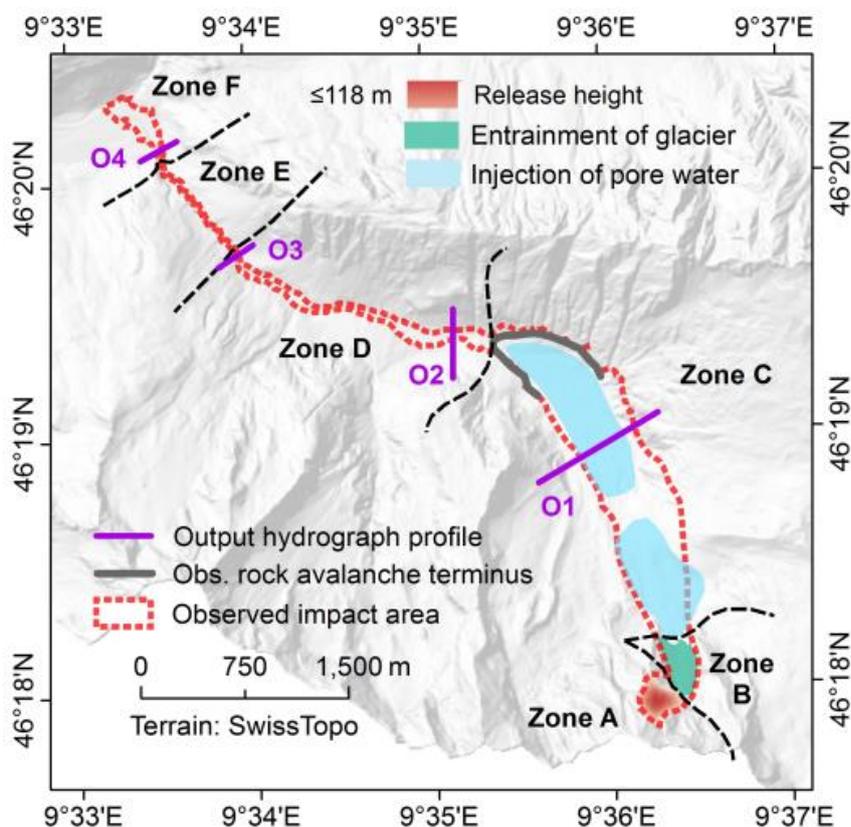
581
Figure 6. Overview of the heights and entrainment areas as well as the zonation performed as the basis for the simula-
tion with r.avaflow. Injection of pore water only applies to the Scenario A. The zones A–F represent areas with largely
homogeneous surface characteristics. The characteristics of the zones and the model parameters associated to each
zone are summarized in Table 1. O1–O4 represent the output hydrograph profiles. The observed rock avalanche ter-
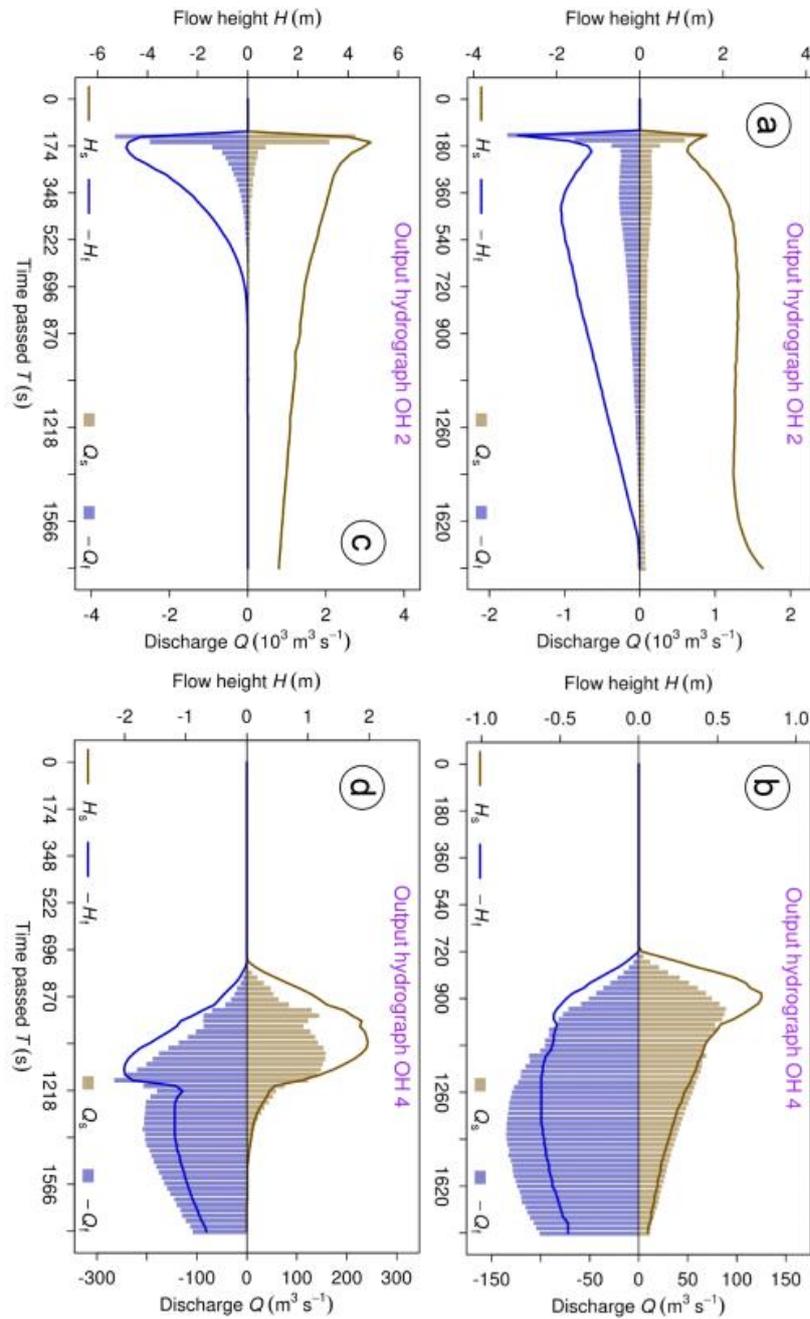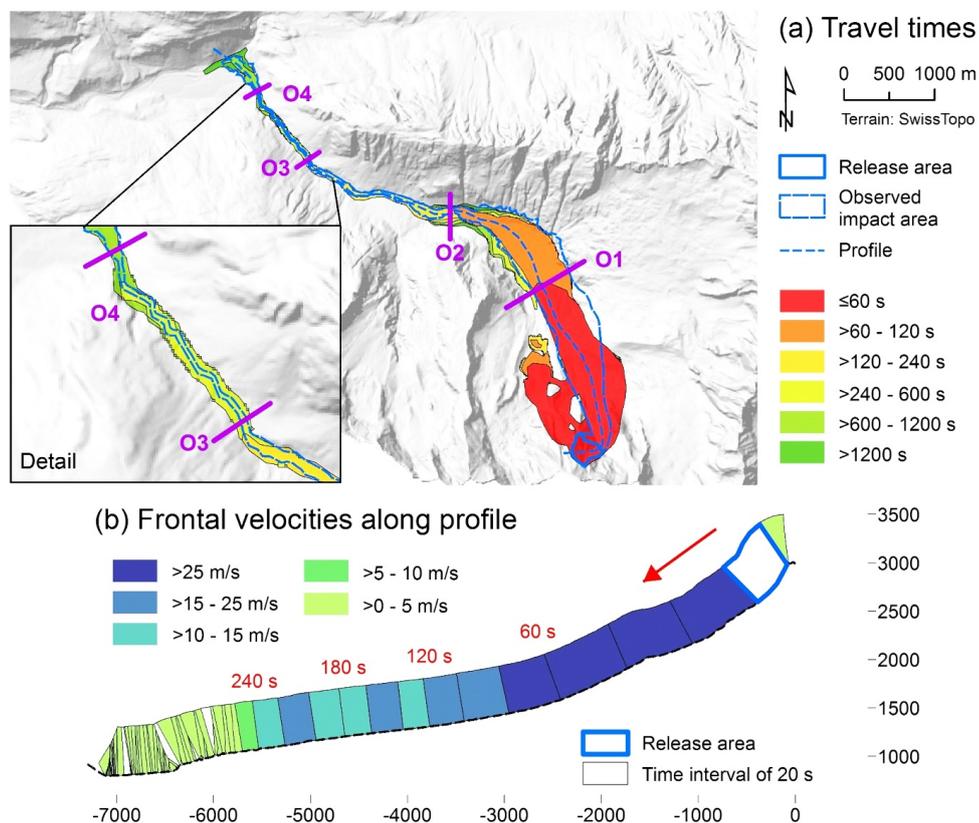minus was derived from WSL (2017).

587
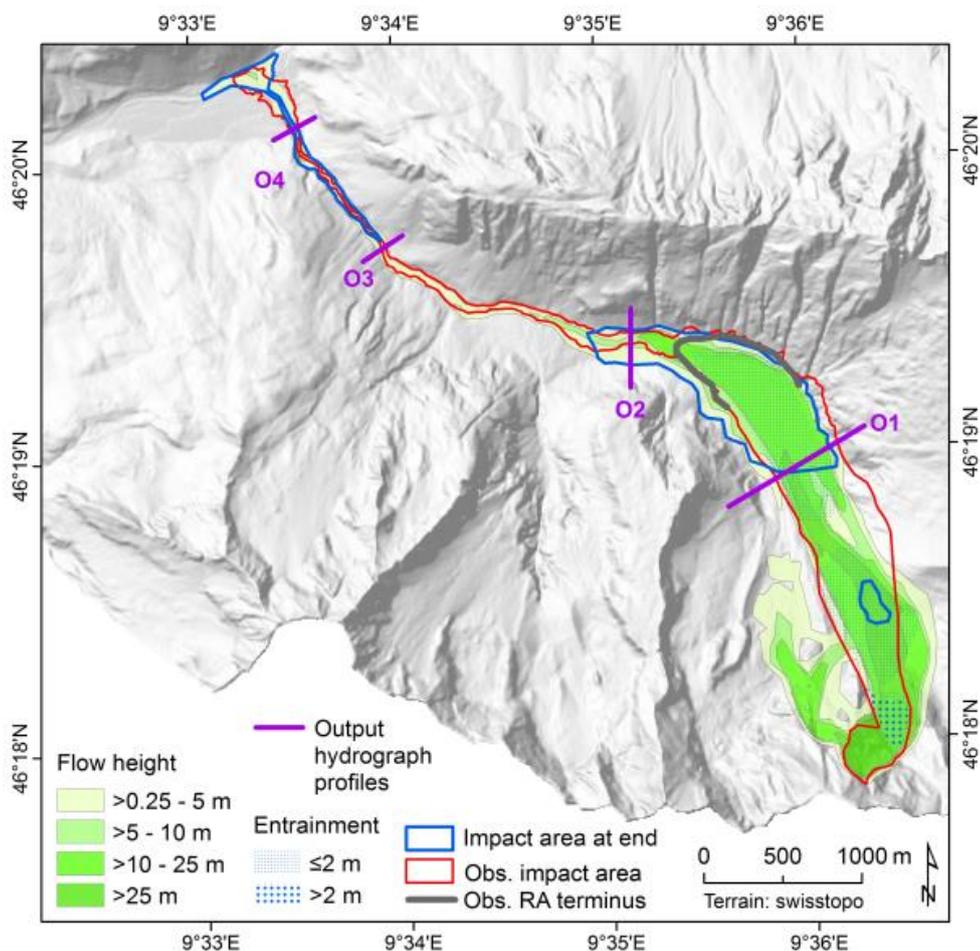
Figure 7. Maximum flow height and entrainment derived for Scenario A. RA = rock avalanche; the observed RA terminus was derived from WSL (2017).
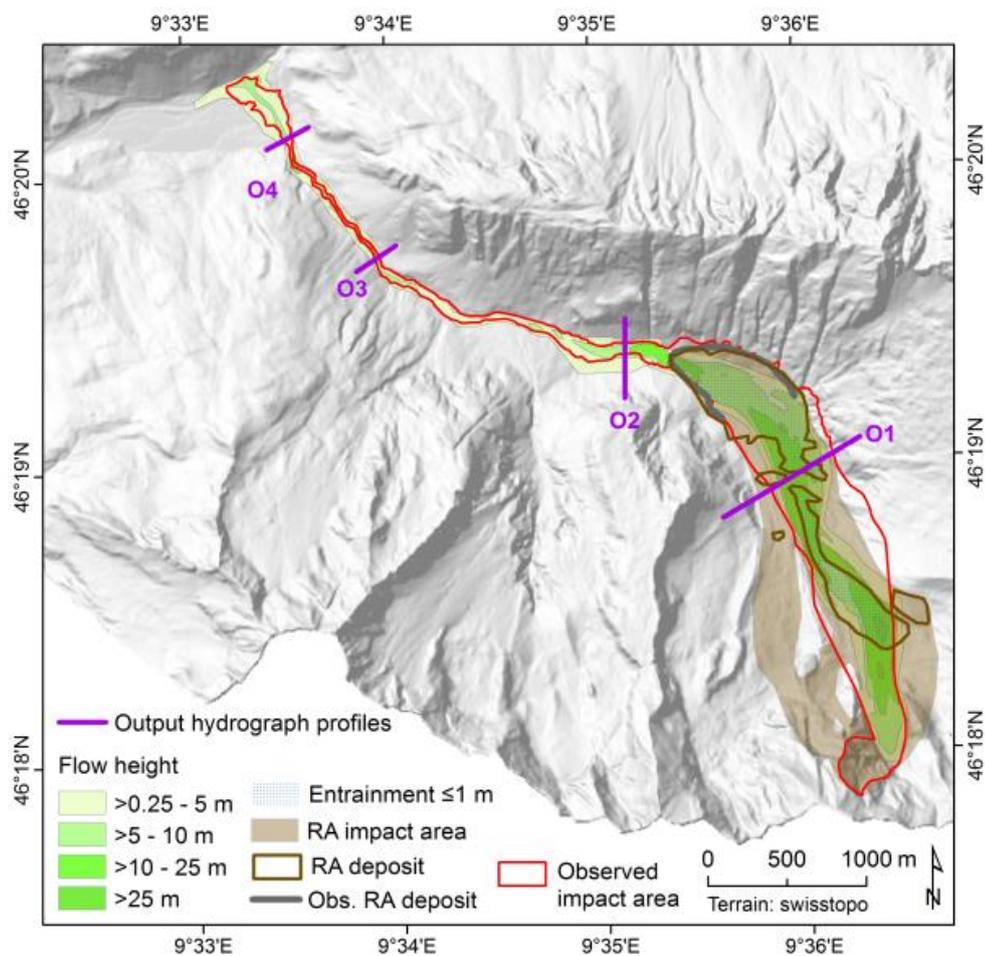
592
593 Figure 8. Output hydrographs OH2 and OH4 derived for the scenarios A and B. (a) OH2 for Scenario A. (b) OH4 for
594 Scenario A. (c) OH2 for Scenario B. (d) OH4 for Scenario B. See Fig. 6 and Fig. 7 for the locations of the hydrograph
595 profiles O2 and O4. H_s = solid flow height; H_f = fluid flow height; Q_s = solid discharge; Q_f = fluid discharge.

596

Natural Hazards
and Earth System
Sciences
Discussions

Open Access

EGU

597
598 Figure 9. Spatio-temporal evolution and velocities of the event obtained for Scenario A. (a) Travel times, starting from
599 the release of the initial rock slide-rock fall. (b) Frontal velocities along the flow path, shown in steps of 20 s. Note that
600 the height of the velocity graph does not scale with flow height. White areas indicate that there is no clear flow path.

601

Natural Hazards
and Earth System
Sciences

Open Access

Discussions

EGU

Figure 10. Maximum flow height and entrainment derived for Scenario B. RA = rock avalanche; the observed RA terminus was derived from WSL (2017).
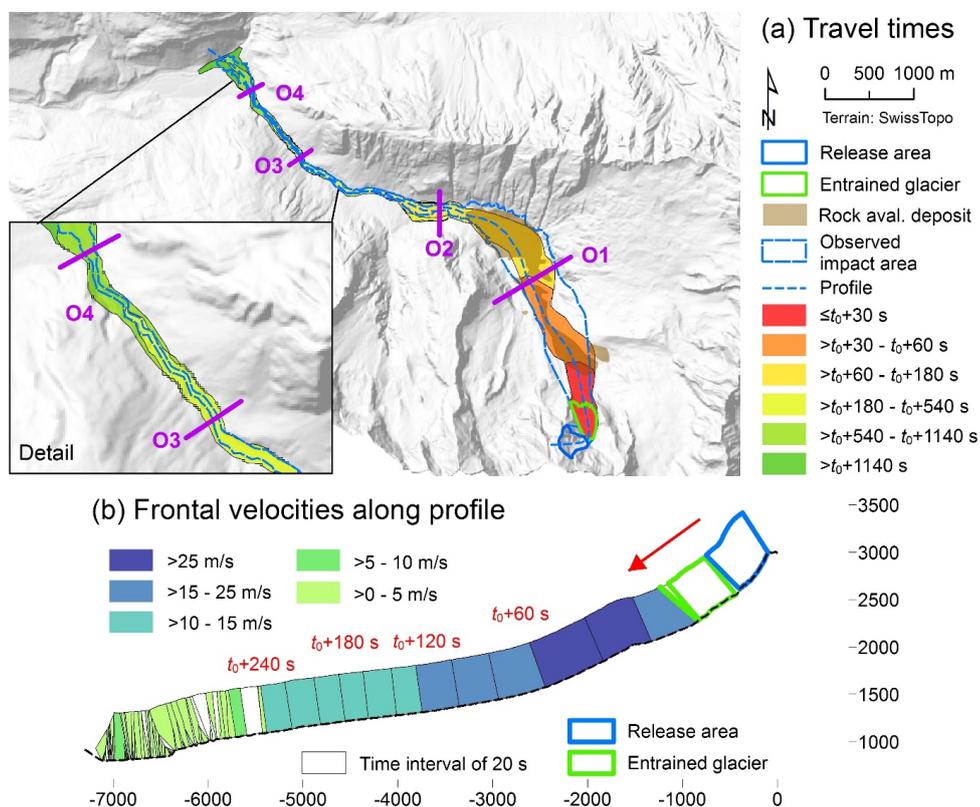
Figure 11. Spatio-temporal evolution and velocities of the event obtained for Scenario B. (a) Travel times, starting from the release of the initial rock slide-rock fall. Thereby t_0 (s) is the time between the release of the rock slide-rock fall and the mobilization of the entrained glacier. (b) Frontal velocities along the flow path, shown in steps of 20 s. Note that the height of the velocity graph does not scale with flow height. White areas indicate that there is no clear flow path.